Stable field emission from nanoporous silicon carbide

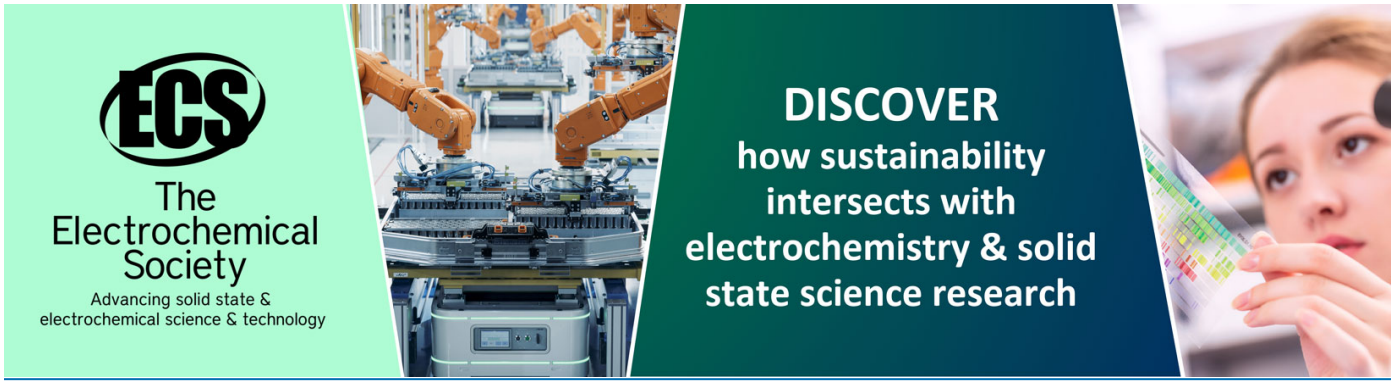

Nanotechnology **24** (2013) 065201 (5pp) doi:10.1088/0957-4484/24/6/065201

Stable field emission from nanoporous silicon carbide

Myung-Gyu Kang[1,2], **Henri J Lezec**[1] **and Fred Sharifi**[1]

[1] The Center for Nanoscale Science and Technology, National Institute of Standards and Technology, Gaithersburg, MD 20899-6204, USA
[2] Maryland NanoCenter, University of Maryland, College Park, MD 20742, USA

E-mail: fred.sharifi@nist.gov

Received 31 October 2012, in final form 9 December 2012
Published 16 January 2013
Online at stacks.iop.org/Nano/24/065201

Abstract
We report on a new type of stable field emitter capable of electron emission at levels comparable to thermal sources. Such an emitter potentially enables significant advances in several important technologies which currently use thermal electron sources. These include communications through microwave electronics, and more notably imaging for medicine and security where new modalities of detection may arise due to variable-geometry x-ray sources. Stable emission of 6 A cm^{-2} is demonstrated in a macroscopic array, and lifetime measurements indicate these new emitters are sufficiently robust to be considered for realistic implementation. The emitter is a monolithic structure, and is made in a room-temperature process. It is fabricated from a silicon carbide wafer, which is formed into a highly porous structure resembling an aerogel, and further patterned into an array. The emission properties may be tuned both through control of the nanoscale morphology and the macroscopic shape of the emitter array.

S Online supplementary data available from stacks.iop.org/Nano/24/065201/mmedia

(Some figures may appear in colour only in the online journal)

1. Introduction

Field emission has been persistently researched for decades, and continuing advances in the design and synthesis of new materials have significantly aided the development of cold electron sources [1–5]. This research is motivated by the distinct technological advantages offered by the desirable properties of field-extracted electrons compared to those that are thermally produced. Attributes such as reduced beam spread and fast response time would allow for significant improvements in a broad array of applications including displays [2], microwave electronics [6] and x-ray sources [7, 8]. These may respectively lead to increased energy efficiency, superior communication and radar and new imaging capabilities for medicine and security. All of these applications require an emitter that is reliable and capable of producing the desired emission current; more critically, the latter two require high emission currents that so far have only been in the realm of thermal sources. Here we report on a new type of field emitter with performance which may potentially enable use in these technologies.

Whereas in thermionic emission electrons are released through heat, field emission extracts electrons using an applied electric field through quantum mechanical tunneling. Electron field emission is described by the Fowler–Nordheim model [9] in which the tunneling barrier is distorted by the large applied electric field. The electron current density J, is expressed as

$$J = \frac{k_1 \beta^2 E^2}{\phi} \exp\left(-k_2 \frac{\phi^{1.5}}{\beta E}\right)$$

where k_1 and k_2 are constants dependent on the properties of the barrier. The current density is exponentially dependent on the emitter's work function ϕ, the applied electric field E and the magnitude of field enhancement caused by the shape of the emitter β. For arrays of emitters, β is defined by a two-level hierarchy: (1) the local electric field enhancement at the level of the individual emitter, set by the size and shape of the local nanostructure, and (2) the global electric field enhancement, set by the larger scale spatial arrangement of the emitters comprising the array. Numerous technologies have been pursued to increase field enhancement at the first

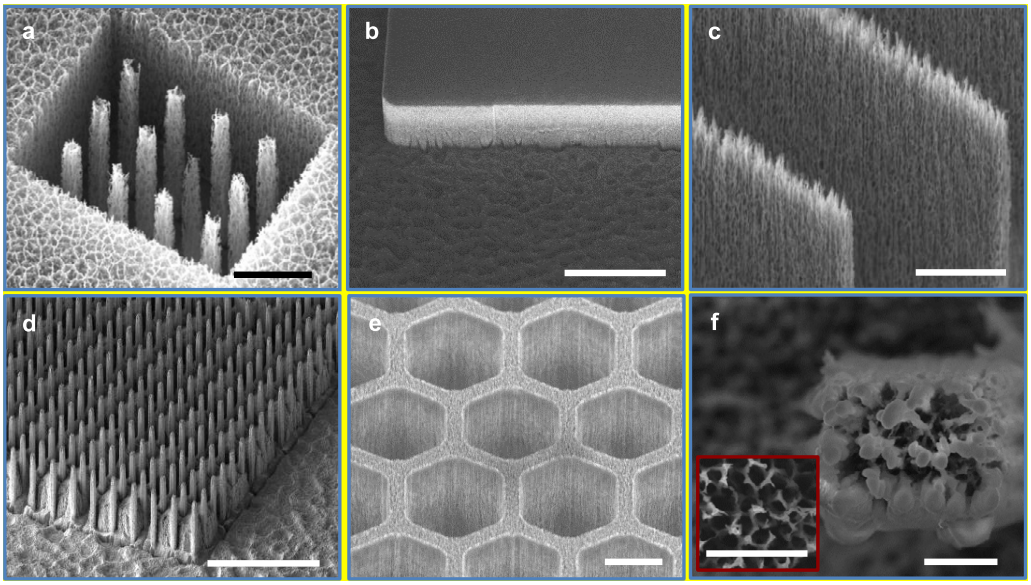

Figure 1. Scanning electron microscopy (SEM) images of various porous SiC emitter structures. (a) Pillar test structure patterned by a focused ion beam (FIB); scale bar 10 μm. (b) Mesa structure fabricated by photolithography and reactive ion etching (RIE); scale bar 50 μm. (c) Magnified view of fin array fabricated by FIB; scale bar 4 μm. (d) Pillar arrays fabricated by FIB; scale bar 50 μm. (e) Hexagonal mesh arrays fabricated by photolithography and RIE; scale bar 10 μm. (f) Pillar structure demonstrating change in morphology due to material decomposition. The inset shows the surface prior to testing; scale bar 1 μm.

level, ranging from early conically shaped tip approaches [1] to more recent efforts focused on carbon nanotubes, with continuing reports of improved performance [10].

Here we demonstrate control of this two-level field enhancement hierarchy in these emitters. These structures are fabricated from highly n-doped silicon carbide wafers which are electrochemically etched into a continuous and highly porous structure. These are subsequently formed by ion etching into a variety of arrays, while maintaining morphology and porosity, as shown in figure 1 and Movies 1 and 2 (available at stacks.iop.org/Nano/24/065201/mmedia). At the local level, field enhancement is defined by the shape of the nanostructure, and varied through electrochemistry conditions so as to alter relevant features such as porosity and wall thickness. At the second level, the macroscopic shape of the emitter array establishes the global field enhancement across the emission area. The starting material, silicon carbide, is chosen as it is refractory and capable of withstanding high current densities. It also possesses a wide bandgap, and these wafers are heavily n-doped. The two properties lead to increased emission by reducing the work function through enhanced electron affinity, as the tunneling process is dominated by electrons in the upper conduction band.

2. Experiment

Wafers of 6-H poly-type, with nominal resistivity ranging from 0.02 to 0.2 Ω cm were etched into porous structures, detailed in the Appendix. We have explored a range of electrochemical conditions, and the resulting structures are dependent on the specifics of the anodization chemistry. This difference in nanostructure morphology manifests itself in the emission characteristics, as it leads to different local field enhancement. As an example, figures 2(a) and (b) demonstrate the variation in structure that results from wafers anodized using electrochemical solutions with different conductivities. In the first (Condition 1), the etching conditions produce structures with wide variations in pore size, and pore wall thickness ranging from 30 to 200 nm, where the thicker pore walls dominate the structure (figure 2(a)). In the second (Condition 2), more oriented structures with smaller wall thickness were produced, with typical pore sizes of 150 nm and wall thicknesses between 20 and 30 nm (figure 2(b)).

These surface emitters were tested in the large-area diode configuration described in the Appendix. As field enhancement requires high aspect ratio structures, the thinner average pore walls of wafers processed through Condition 2 should ideally lead to higher emission. This is indeed observed, as shown in figure 2(c), where the emission characteristics corresponding to the two conditions are plotted. (For comparison, testing was also performed on an unprocessed wafer, demonstrating no significant emission.)

Further field enhancement may be achieved through design of the larger scale structure of the emitting array. For this goal, a variety of exploratory structures were fabricated to assess the mechanical robustness and the limits of the aspect ratio that could be achieved (figure 1). The anodized structures were initially plasma etched into macroscopic mesas (figure 1(b)) and formed into shaped arrays using lithographically defined etch masks, or through a high resolution focused ion beam (FIB). Compared to the original mesa, the area is reduced by 85% for the fin array (figure 1(c)) and 96% for the pillar array (figure 1(d)). The fin and pillar arrays were formed from a starting square mesa (figure 1(b)) with a lateral dimension more than 10 times

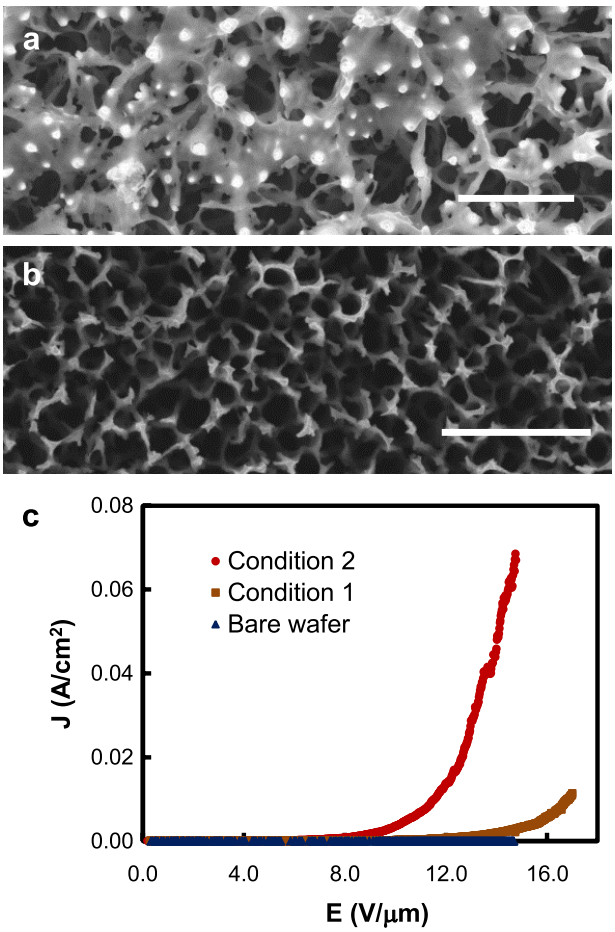

Figure 2. Top: SEM images of an electrochemically etched wafer using two different conditions and the measured current densities (J) versus applied electric field (E). (a) Condition 1; scale bar 1 μm. (b) Condition 2; scale bar 1 μm. (c) Resulting J versus E curves for Conditions 1 and 2, and an unprocessed wafer.

the pitch or the height of the emitter, detailed in Appendix. This relative scaling is important for the measured current density to accurately represent larger sized arrays, and thus be macroscopic. Thus all current densities reported here are calculated using the macroscopic dimensions of the emitter array, defined by the lateral dimensions of the starting mesa.

3. Results and discussion

In contrast to the surface emitters formed solely by wafer anodization (figures 2(a) and (b)), electron emission in the patterned structures occurs at lower electric fields, and is initially dominated by emission from the array's perimeter due to this region's higher electric field enhancement. In the test procedure, the field is increased until the current density from this perimeter region exceeds the material's inherent capability (discussed below), at which point the emission drops as the nanostructure becomes compromised. Consequently, the perimeter field is diminished, the array emits more uniformly across the entire structure, and the current continues to rise with increasing electric field. Since this emission is now over a larger area, significant stable emission may be obtained, and the fields required to reach the material limit in this regime are higher. Figures 3(a)–(d) detail the perimeter and areal emission characteristics of a mesa (figure 1(b)) and a pillar array (figure 1(d)), demonstrating this effect. Post-testing scanning electron microscopy at various stages of the test indicates that the likely failure mechanism is a morphology change in the structure (figure 1(f)). It is manifested as rounding of the nanostructure surface, suggesting decomposition of the silicon carbide. Our results indicate that the emission is stable so long as the material's inherent limit is not exceeded. Finally, in figure 4 the areal emission characteristics of the mesa, fin and pillar arrays (figures 1(b)–(d)) are shown, demonstrating the second-level field enhancement arising from the global structure of the array. We note that the pillar array (figure 1(d)) produced stable emission in excess of 6 A cm^{-2} at 7.5 V μm^{-1}, a value that compares favorably with carbon nanotube emitters [10], and is at the level of standard thermal sources [11].

Several lifetime and reliability measurements have been undertaken to ascertain the robustness of these structures. We have performed both continuous pulse and dc testing, and the results indicate that (areal) emission is robust so long as the current densities remain below where material decomposition occurs. For our experimental configuration, the fields required to reach this material limit may be readily obtained for the pillar array (figure 1(d)). As shown in figure 4(c) (inset), the emission fluctuates and becomes unstable at a current density above 7 A cm^{-2}, and post-test SEM examination indicated material decomposition (figure 1(f)).

To assess reliability at high current densities below the decomposition point, a mesa emitter was repeatedly subjected to a slow dc ramping of the electric field detailed in figure 3(b), and showed no changes over an hour's operational time. Further, testing has also been performed on mesh arrays with 30% of the area of the starting mesa (figure 1(e)). This structure was subjected to sequences of dc pulses of applied voltage, each being pulse approximately 5 s long, with varying off times between each pulse (60, 100 and 200 s). As shown in figure 5(a), the emission does not vary as long as the emitter is allowed sufficient time (200 s) to cool to its original temperature, and shows only a slight increase in emission within the pulse duration (figure 5(a), inset). As the off-time is decreased to 100 and 60 s and the emitter temperature is allowed to rise (figures 5(b) and (c)), the overall emission increases accordingly and the enhancement within a pulse is more pronounced. The results show that the dc emission levels consistently exceed 1 A cm^{-2} during this demanding test protocol. At the highest current densities, local heating resulted in the emitter exhibiting a faint reddish glow during the pulse. The emitters recover to initial levels once they are allowed to cool. This test procedure also resulted in an overall emission time of approximately an hour.

4. Conclusion

With further optimization of materials and processes, the promising performance reported in these initial studies raises the realistic possibility of field emitters as a potential

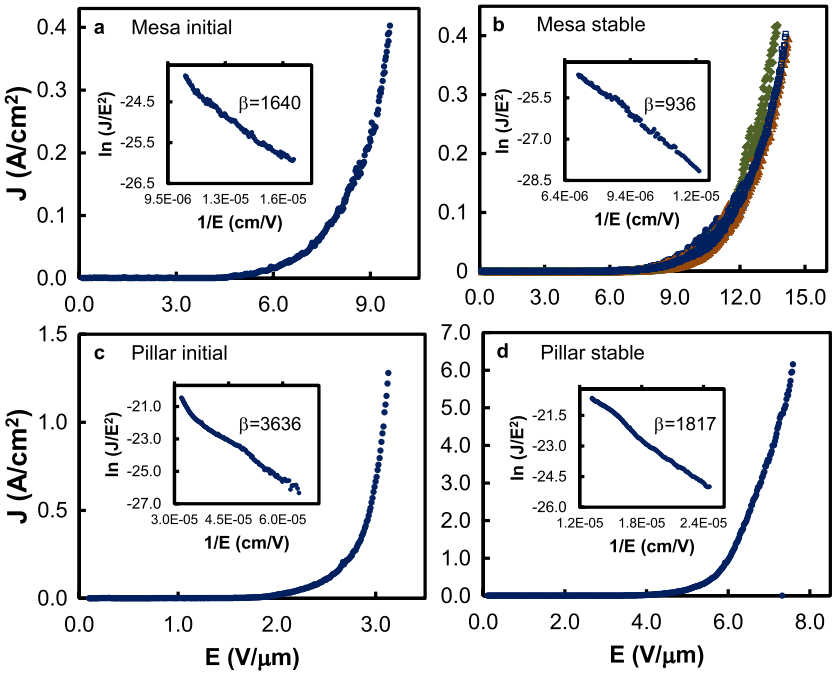

Figure 3. *J* versus *E* and corresponding Fowler–Nordheim (FN) plots (inset) of the mesa and pillar structures. (a) Initial emission tests dominated by the perimeter of a mesa. (b) Stable areal emission characteristics of the same mesa. For (b) six different *J* versus *E* data sets were measured at various electrode separations ranging from 0.24 to 1.35 mm. In each curve, the voltage was continuously ramped to the maximum value and then decreased, in increments of 20 V steps every 0.5 s. (c) Initial tests of a pillar array, dominated by perimeter emission. (d) Stable areal emission of the same pillar array. The FN inset shows the extracted β values.

replacement for thermal sources. We believe the robustness is partly due to the monolithic nature of the structures, as there are no material interfaces that may be potential failure points. In addition, the porous morphology leads to a continuous supply of emission points as the emitting surface wears. Both should prove to be advantageous for performance and reliability. We are cautiously optimistic that performance characteristics may be further enhanced through improvements of electrochemistry conditions and geometric design, towards realization of an effective cold cathode technology capable of producing a high current.

Acknowledgments

The authors thank Dr Rachel Cannara for numerous insightful discussions. M-GK acknowledges support under the Cooperative Research Agreement between the University of Maryland and the National Institute of Standards and Technology, the Center for Nanoscale Science and Technology, through award 70NANB10H193.

Appendix

A.1. Fabrication

The porous silicon carbide structures tested were produced by electrochemical etching using two processing conditions, and are similar to a previous report [12]. In Condition 1, the anodizing solution consisted of 10% HF and 5% ethanol (by mass) with the balance distilled water. In Condition 2, the anodization solution consisted of 20% HF and 5% ethanol (by mass) with the balance de-ionized water. Ohmic contact to the backside (silicon face) of the wafer was formed using Ni (50 nm), annealed at 300 °C in Ar. The etched side (carbon face) was subsequently anodized at 20 V using a Pt mesh counter-electrode, at a nominal rate of 4 μm min^{-1}. The use of de-ionized water in Condition 2 resulted in a dense top layer approximately 2 μm thick with low porosity. This top layer was subsequently removed by reactive ion etching (RIE) using 90% SF_6 and 10% O_2 plasma etching, exposing an underlying structure with more uniform porosity and smaller wall thickness than wafers anodized using Condition 1.

The structure shown in figure 1(b) is a square mesa 210 μm per side. It was fabricated through the formation of the nanoporous structure on a SiC wafer, and subsequently patterned with a metal etch mask through conventional photolithography, and RIE etched as before. This mesa fabrication procedure was also used for fabrication of the fin and pillar arrays shown in figures 1(c) and (d). Here, the mesas were further patterned by FIB etching (Ga+ ions, 30 keV beam energy, 2.5 nA beam current, 50 nm nominal beam diameter) assisted by XeF_2 gas. Compared to FIB milling without gas, the use of gas-assisted etching (GAE) in shaping emitters in porous SiC leads to a significant increase in the material removal rate (by a factor of ∼6). In figure 1(c), the fins comprising the array are 1.5 μm wide and 20 μm high, with 10 μm pitch. In figure 1(d), the square pillars are 2 μm per side and 20 μm high, with the same pitch. In figure 1(e), the mesh structure array is 0.5 mm per side, and has hexagonal sides 10 μm long, 2.3 μm wide and 20 μm high, fabricated by the RIE process outlined above.

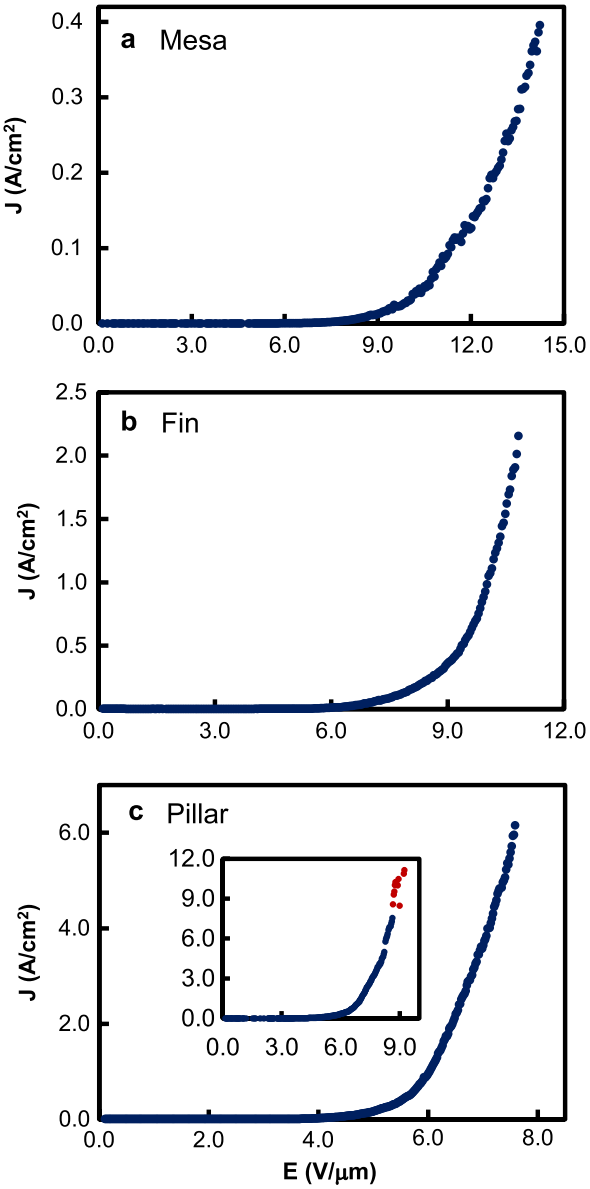

Figure 4. J versus E plots of patterned structures showing emission enhancement through macroscopic geometric design of the emitter array for a mesa (figure 1(b)), fin (figure 1(c)) and pillar (figure 1(d)) array. The turn on fields, defined for a current of 10 μA, are 4.4 V μm^{-1}, 6.5 V μm^{-1} and 9.6 V μm^{-1} for the pillar, fin and mesa structures respectively. Inset to (c): J versus E extended to the failure point of the pillar array, demonstrating emission instability (red) as the material limit is reached.

A.2. Testing and analysis

The test apparatus has parallel-plate geometry and is in a vacuum chamber with a base pressure of 1.3×10^{-7} Pa; testing was typically initiated at 1×10^{-6} Pa. The anode and cathode are 1 cm in diameter. The electrode separation is controlled precisely as it determines the electric field value, and is typically 1.000 mm $\pm$ 0.002 mm. The measurements were performed either in sequential dc or pulse mode, with pulse widths ranging from 0.2 to 10 ms and a typical frequency of 1 Hz. The emission results were independent of the pulse widths. The pulse data shown in figures 2(c), 3(a), (c), (d) and 4(b), (c) were obtained using a 0.2 ms square pulse at a frequency of 1 Hz. The uncertainty in electric field is 0.2% (1σ) and is determined by the uncertainties in the electrode separation and output of the high voltage apparatus. The uncertainty in the emission current is 0.1% (1σ) and is determined by the precision of the current measurement apparatus. For the extraction of β through FN data analysis, the values used for the constant of integration and work function are $k_2 = 6.83\times10^7$ eV$^{-3/2}$ V cm^{-1} and $\phi = 4.2$ eV, respectively.

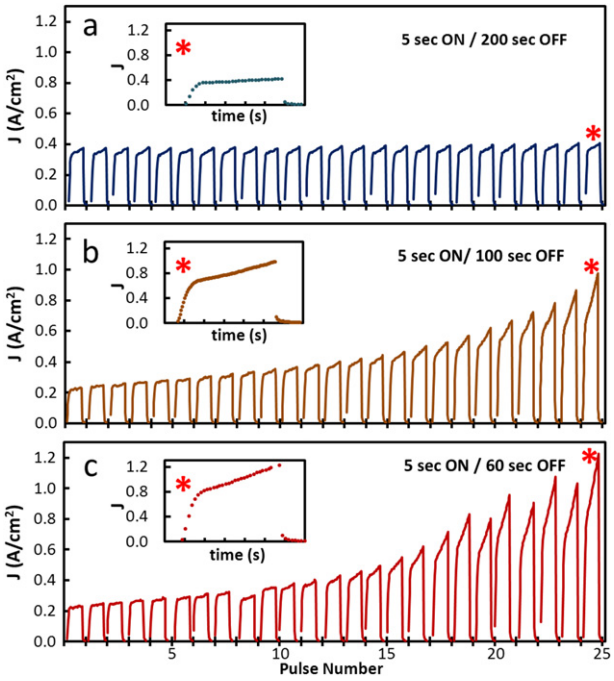

Figure 5. Emission versus pulse number for testing of the mesh structure shown in figure 1(e). Each pulse is 5 s in duration. The off times in the pulse sequence are not shown to ease comparison between results. The off times are 200, 100 and 60 s for (a), (b) and (c), respectively. The insets show the emission profile during a pulse, at the end of the pulse sequence (denoted by '*'); time intervals in the insets are 1 s.

References

[1] Spindt C A 1968 *J. Appl. Phys.* **39** 3504–5
[2] de Heer W A, Châtelain A and Ugarte D 1995 *Science* **270** 1179–80
[3] Fan S, Chapline M G, Franklin N R, Tombler T W, Cassell A M and Dai H 1999 *Science* **283** 512–4
[4] Hsu D S Y and Shaw J 2002 *Appl. Phys. Lett.* **80** 118–20
[5] Teo K B K, Minoux E, Hudanski L, Peauger F, Schnell J P, Gangloff L, Legagneux P, Dieumegard D, Amaratunga G A J and Milne W I 2005 *Nature* **437** 968
[6] Jensen K L 1999 *Phys. Plasmas* **6** 2241–53
[7] Wang G, Yu H and De Man B 2008 *Med. Phys.* **35** 1051–64
[8] Schwoebel P R 2006 *Appl. Phys. Lett.* **88** 113902
[9] Fowler R H and Nordheim L 1928 *Proc. R. Soc.* A **119** 173–81
[10] Calderón-Colón X, Geng H, Gao B, An L, Cao G and Zhou O 2009 *Nanotechnology* **20** 325707
[11] Cronin J L 1981 *IEE Proc.* **128** 19–32
[12] Ke Y, Devaty R P and Choyke W J 2008 *Phys. Status Solidi* b **245** 1396–403